Quantitative Imaging of Lymphatic Function with Liposomal Indocyanine Green

Steven T. Proulx[*], **Paola Luciani**[*], **Stefanie Derzsi**, **Matthias Rinderknecht**, **Viviane Mumprecht**, **Jean-Christophe Leroux**, and **Michael Detmar**
[1]Institute of Pharmaceutical Sciences, Swiss Federal Institute of Technology, ETH Zurich, 8093 Zurich, Switzerland

Abstract

Lymphatic vessels play a major role in cancer progression and in postsurgical lymphedema, and several new therapeutic approaches targeting lymphatics are currently being developed. Thus, there is a critical need for quantitative imaging methods to measure lymphatic flow. Indocyanine green (ICG) has been used for optical imaging of the lymphatic system but it is unstable in solution and may rapidly enter venous capillaries after local injection. We developed a novel liposomal formulation of ICG (LP-ICG), resulting in vastly improved stability in solution and an increased fluorescence signal with a shift towards longer wavelength absorption and emission. When injected intradermally to mice, LP-ICG was specifically taken up by lymphatic vessels and allowed improved visualization of deep lymph nodes. In a genetic mouse model of lymphatic dysfunction, injection of LP-ICG showed no enhancement of draining lymph nodes and slower clearance from the injection site. In mice bearing B16 luciferase expressing melanomas expressing vascular endothelial growth factor-C (VEGF-C), sequential near infrared imaging of intradermally-injected LP-ICG enabled quantification of lymphatic flow. Increased flow through draining lymph nodes was observed in mice bearing VEGF-C expressing tumors without metastases while a decreased flow pattern was seen in mice with a higher lymph node tumor burden. This new method likely will facilitate quantitative studies of lymphatic function in preclinical studies and may also have potential for imaging of lymphedema or improved sentinel lymph detection in cancer.

Keywords

Lymph node; near-infrared; lymphangiogenesis; liposome; metastasis

INTRODUCTION

The lymphatic vascular system has recently garnered an increasing amount of attention as its diverse roles in tumor metastasis, chronic inflammation, and lymphedema have been better understood (1–2). In particular, there is increasing evidence that tumor-associated lymphatic vessel growth promotes lymph node metastasis (3–5) and that tumor-induced lymphangiogenesis within sentinel lymph nodes enhances further metastatic spread (6–8). Since novel therapeutic approaches for the treatment of tumor lymphangiogenesis, as well as for the therapy of postsurgical lymphedema in cancer patients are currently developed, there

Correspondence: Michael Detmar, M.D., Institute of Pharmaceutical Sciences, Swiss Federal Institute of Technology, ETH Zurich, Wolfgang-Pauli-Str. 10, HCI H303, CH-8093 Zürich, Switzerland, Tel.: ++41-44-633-7361, Fax: ++41-44-633-1364, michael.detmar@pharma.ethz.ch.
[*]These authors contributed equally to this work

is a critical need for quantitative imaging methods to measure lymphatic function and to quantify lymphatic flow.

Lymphatic imaging has traditionally been performed clinically with direct lymphangiography methods using computed tomography or lymphscintigraphy with 99m technetium bound to either sulfur colloid or albumin (9). These methods have several shortcomings, particularly when applied to animal models. These include the need to directly inject contrast agent into lymphatic vessels, the use of radioactive tracers and poor anatomical spatial resolution (9). More recently, magnetic resonance imaging (MRI) methods that can detect gadolinium or iron based contrast agents in lymphatic vessels and within lymph nodes have been developed (10–14). However, the costly and technically demanding nature of MRI, especially when applied to preclinical research, has led to investigation of alternative modalities to image the lymphatic system.

Fluorescence imaging methods focusing on contrast agents that have spectral properties in the near infrared (NIR) region have recently shown great promise for lymphatic imaging (15–16). NIR light, in the wavelength range between 700 and 900 nm, allows deeper penetration of photons into living tissue due to reduced absorption and scattering and minimal tissue autofluorescence (17). The NIR dye indocyanine green (ICG) has been FDA approved, as an agent to evaluate hepatic function, cardiac output, and for ophthalmic angiography (16,18). ICG binds quickly to serum albumin after intravenous injection and is rapidly cleared through the liver and bile duct (19–21). Recent studies have demonstrated the potential of this dye to image lymphatics in animal models and in humans (22). However, there are several aspects of the dye that make it nonideal for quantitative lymphatic imaging. First, ICG is unstable in solution. It aggregates and self-quenches (23) and therefore must be injected within hours as it otherwise rapidly loses its fluorescence. *In vivo*, plasma proteins, such as albumin, bind preferentially to the monomeric ICG molecules and reduce the aggregation (24–25). Thus, prevention of aggregation of ICG is dependent on the availability of plasma proteins at the injection site, placing a limitation on the concentration that can be administered. Second, the quantum yield of ICG is inherently low, although this is improved to some extent with protein binding (26). Third, because of its low molecular weight, ICG rapidly leaks out of collecting lymphatics into the extravascular space or is being taken up by venous capillaries at the site of injection or by high endothelial venules within the lymph nodes. For these reasons, ICG has been complexed to human serum albumin (HSA) prior to injection, improving the optical characteristics and preventing aggregation (26–27). In attempts to increase ICG stability in biological fluids without altering its biocompatibility, the dye has been encapsulated in PLGA nanoparticles (28) or conjugated to polyether polyol dendrons (29).

Colloidal particles can interact with ICG and induce changes in spectral properties (27,30). For instance, it was found that large phospholipid vesicles reduced the dye's self-quenching and slightly increased its quantum yield (30). More recently, ICG was stabilized by its association to surfactant micelles (31). Despite interesting *in vitro* data, the *in vivo* efficacy of these systems has not been assessed so far. In the case of micelles, their dilution following injection may rapidly induce their dissociation (32) and premature release of ICG. Owing to their well established safety profile, stability upon dilution, small size and versatility in terms of composition and surface-properties, we hypothesized that liposomes might constitute a promising vehicle to image the lymphatic system.

In this study, we designed a liposomal formulation of ICG (LP-ICG) that possesses ideal attributes for lymphatic function imaging. We found that the LP-ICG displays improved optical properties and prolonged fluorescence stability in solution over weeks. After intradermal injection, several draining lymph nodes were clearly visualized allowing the

dynamics of lymphatic flow to be quantified. Quantitative imaging of lymphatic function with LP-ICG was further validated in a genetic model of lymphatic dysfunction and in a B16 melanoma tumor model of lymphatic metastasis.

MATERIALS AND METHODS

Chemicals

ICG (IR-25, laser grade pure) was purchased from Acros Organics (Geel, Belgium). 1,2-oleoyl-*sn*-glycero-3-phosphocholine (DOPC) and 1,2-distearoyl-*sn*-glycero-3-phosphoethanolamine-*N*-[methoxy(polyethylene glycol)-2000] (PEG-DSPE) were a gift from Lipoid GmbH (Ludwigshafen, Germany). D-(+)-Glucose monohydrate and HSA (97–99% purity) were purchased from Sigma Aldrich (St. Louis, MO). Chloroform (analytical grade, Fluka, St. Louis, MO) and dimethyl sulfoxide (DMSO) (Uvasol®, spectroscopic grade, Merck, Darmstadt, Germany) were used as received.

Liposome preparation

Liposomes were prepared by the film-hydration/extrusion method (33). DOPC and PEG-DSPE (95:5 mol %, 3.9 mM total lipid concentration) were co-dissolved in chloroform. The organic solvent was eliminated under nitrogen and the lipid film placed under vacuum overnight. The dried film was then hydrated with an isotonic glucose solution (5% *w/v*) containing ICG (15 μM, lipid/dye molar ratio of 260). The ICG-containing dispersion was freeze-thawed 6 times and extruded 10 times through double stacked 50-nm pore size polycarbonate membranes using a Lipex thermobarrel extruder (Northern Lipids, Burnaby, BC, Canada) to yield small unilamellar vesicles. Free dye was removed by size exclusion chromatography on a PD MidiTrap G-25 column (GE Healthcare, Little Chalfont, UK) using glucose buffer as eluent.

Filtered liposomes had a mean diameter of 58.8 nm ± 1.8 nm (n=6) as measured by dynamic light scattering (DelsaNano Zetasizer, Beckmann-Coulter Inc., Fullerton, CA), adjusting viscosity and refractive index as needed (34). The encapsulation efficiency was determined by spectrophotometry in a Cary 300 Bio UV-visible spectrophotometer (Varian Inc., Palo Alto, CA) after a 10-fold dilution of the samples in DMSO. It was 96 ± 7 %.

Formulation stability

Absorbance and fluorescence measurements were performed over 42 days on a Infinite M200 microplate reader (Tecan Ltd., Männedorf, Switzerland) using black/clear (flat bottom, untreated) Optilux 96-well plates (BD Biosciences, San Jose, CA). The scanned visible range was 600–900 nm. The set parameters for the fluorescence scans were: $\lambda_{ex} = 720$ nm, $\lambda_{em} = 750–850$ nm (manual gain optimization). During the time of observation, ICG-containing formulations were stored in the dark at room temperature. Stability of free and encapsulated ICG was monitored in a serum-containing medium (FBS mixed at 50% *v/v* with isotonic glucose) over 12 h. Fluorescence spectra were recorded on a Cary Eclipse Fluorescence spectrophotometer (Varian Inc., Palo Alto, CA), equipped with a Peltier circulating water bath to strictly control the temperature. Serum-induced bilayer destabilization was monitored using a fluorescence dequenching assay (details provided as Supplemental Methods). DOPC/PEG-DSPE liposomes were incubated in media containing a high or low concentration of serum (50% or 10% FBS, respectively) and the release kinetics was monitored over 3 h at 37°C.

Mice

C57BL/6J-*Tyr*^{c-J} albino mice (Jackson Laboratories, Bar Harbor, ME) were maintained in pathogen free conditions until imaging. NMRI mice with a mutation in VEGFR3 (*Chy* mice)

were a kind gift of Dr. Kari Alitalo, University of Helsinki (35). Mice were fed an alfalfa-free diet (Experimental diet #2222, Provimi Kliba, Penthalaz, Switzerland) to reduce tissue autofluoresence. All animal experiments were approved by the cantonal veterinarian office Zurich (Kantonales Veterinäramt Zürich; protocol 128/2008).

B16 murine melanoma model

B16.F10-luc2 murine melanoma cells were purchased from Caliper Life Sciences (Alameda, CA). Cells were maintained in culture with DMEM medium (Invitrogen, Carlsbad, CA) containing 10% FBS. Cells were transfected by electroporation with full-length human VEGF-C subcloned into the pcDNA3.1 (Invitrogen) vector. Stable clones (B16.F10-VEGF-C cells) were selected and human VEGF-C expression was confirmed by RT-PCR and ELISA in comparison to B16.F10.pcDNA empty vector transfected cells. We detected 0.8 ng/ml of human VEGF-C in the cell culture supernatant of the stably VEGF-C transfected clone that was used for further studies, as assessed by quantitative ELISA (Bender MedSystems, Vienna, Austria) at 24 hours after seeding 1×105 cells. These levels are similar to those reported for the highly metastatic PC3 human prostate tumor cell line (36–37). B16.F10-VEGF-C or B16.F10.pcDNA cells (2×10^5) in 10 μL PBS were injected into the right footpads of 9- to 11-week-old female C57BL/6J-Tyr^{c-J} mice (38). The tumors were allowed to grow for 21 days at which time they reached a diameter of approximately 6 mm.

In vivo near infrared fluorescent (NIRF) imaging

Mice were anesthesized with 2% isoflurane and the fur was removed from the leg and abdomen using a shaver and topical hair remover cream. The mice were then positioned inside an IVIS Spectrum (Xenogen, Caliper Life Sciences) on their ventral side and pre-contrast injection images were taken to establish background signal intensities at the tissues of interest. The imaging parameters were: $\lambda_{ex} = 745$ nm, $\lambda_{em} = 840$ nm, exposure time 2 to 6 s, f/stop 2, medium binning, field of view 6.6×6.6 cm^2. Five μL of either ICG dye or the ICG liposomes (15 μM in 5% glucose each) were intradermally injected at the top of the foot. Immediately after injection, serial images were acquired every 30 s for 10 min and every 60 s thereafter. Total acquisition time varied from 25 to 70 min depending on the model. Imaging of the site of injection was performed with the above settings, but with exposure time of 0.1 s.

For image analysis, Living Image software (Caliper Life Sciences) was used. Regions of interest (ROI) were placed over the popliteal lymph node, medial iliac lymph node (when visible), and liver. Average signal intensity values were recorded for each ROI and plotted versus time in Graphpad Prism. For assessments of flow through the popliteal lymph node, the data were analyzed *via* normalizing the values based on a percent of total enhancement (maximum average ROI signal intensity minus baseline average ROI signal intensity). Beginning at the time point of maximum enhancement in the popliteal lymph node, the data was fit to an exponential decay model:

$$\text{Normalized Signal Enhancement} = \text{Span} * e^{-K_{LN}t} + \text{Plateau}$$

with maximum signal enhancement = 1 at time = 0 and a plateau = 0 this reduces to:

$$\text{Normalized Signal Enhancement} = e^{-K_{LN}t}$$

The rate of signal decay in the lymph node be expressed by either K_{LN} or by half life (= $0.67 / K_{LN}$).

In vivo bioluminescent imaging

The IVIS Spectrum was also used for *in vivo* bioluminescent imaging of B16-F10-luc2 tumors and draining lymph node metastases. Mice were injected intraperitoneally with 150 mg/kg body weight D-luciferin substrate (Caliper Life Sciences,). Pilot studies revealed that the peak bioluminescent intensity of tumors was reached at approximately 25 min after D-luciferin injection, therefore this timepoint was chosen for imaging. Images of the footpad tumor were taken under the following settings: exposure time 5 s, f/stop 1, medium binning, field of view 6.6×6.6 cm^2. Afterwards, the tumor was covered with black tape and one image (exposure time 3 min, f/stop 1, medium binning, field of view 3.9×3.9 cm^2) of the region comprising the popliteal lymph node was collected. On the final day of imaging, mice were sacrificed *via* cervical dislocation and images of the dissected lymph nodes were taken with exposure time of 1 min. Living Image software was used to quantify the bioluminescent signal, reported as units of tissue radiance (photons/s/cm^2/sr).

Statistics

Mean and standard deviation are reported for all data. Comparisons between two groups at the same timepoints were made with two-tailed t-tests. Comparisons between multiple groups or multiple timepoints were made with two-way ANOVA analyses. Spearman rank correlations were made to test for association between two variables.

RESULTS

Spectral properties and stability of LP-ICG

Several liposomal formulations differing in composition, size and loading procedures were first screened (data not shown). Figure 1 shows the absorption (A) and fluorescence (B) spectra of ICG dissolved in isotonic glucose buffer compared to the spectra of optimized LP-ICG (DOPC/PEG-DSPE 95:5 mol/mol, 60 nm) (C). The remarkable red shift (22 nm) in the absorption spectrum of ICG liposomes confirmed the affinity of ICG for lipid bilayers (24–25). The emission spectrum of the ICG-loaded lipid dispersion exhibited a 4-fold increase in fluorescence intensity, as well as an expected red shift in $\lambda_{max,em}$. The seemingly minor shifts toward longer wavelengths resulted in a dramatic decrease of *in vivo* background signal during detection (Figure S1), leading to an improved signal-to-noise *in vivo*.

The optical properties of ICG and LP-ICG were monitored as a function of time. As illustrated in Figure 1D, the free ICG completely lost its fluorescence signal within 7 days. In contrast, the LP-ICG was highly stable with unaltered spectral properties for almost 14 days. The impact of HSA on the spectral properties of ICG and LP-ICG was then compared. At an HSA:ICG molar ratio of 1, HSA had no influence on the absorption and emission spectra of LP-ICG (Figure S2). As reported previously, the complexation of HSA with free ICG induced a red shift of the maxima which was similar to the one observed upon the encapsulation of ICG in liposomes, but the fluorescence intensity remained 2-fold lower. In order to assess the stability of the liposomal bilayer, the liposomes were incubated in media containing either a high or low concentration of serum (50% or 10% FBS, respectively), and leakage was monitored using a fluorescence dequenching assay (Figure S3). The high serum concentration was used to mimic the blood, while the low serum concentration was used as a surrogate of the lymph. At the low serum concentration, we found that less than 10% of the ICG content was released within 3 h, indicating that the liposomes maintained their integrity. In contrast, there was a rapid destabilization at high serum concentrations, suggesting that the liposomes are not stable in the systemic circulation.

In vivo imaging of C57BL/6 albino mice

LP-ICG was compared to ICG after intradermal injection into the paws of normal C57BL/6 albino mice. Surprisingly, no major differences in the dynamics of flow of the contrast agents through the popliteal lymph node were seen in the initial hour postinjection (Figure 2) despite the larger hydrodynamic diameter (~60 nm) of LP-ICG. Both imaging agents demonstrated extremely rapid enhancement of the popliteal lymph nodes, indicating that the increased interstitial pressure created by the injection volume in the intradermal space was sufficient to open gaps between the lymphatic endothelial cells and quickly fill the lymphatic space with contrast agent. There was no significant difference in the signal decay at the popliteal lymph node between groups, indicating that the free ICG did not flow faster through draining lymph nodes than the LP-ICG.

At later timepoints, two major differences were found between ICG and LP-ICG. First, a second draining lymph node, the medial iliac, was visualized repeatedly after LP-ICG injection but never seen with ICG. This lymph node is much deeper (~1 cm) compared to the popliteal lymph node (39). Second, LP-ICG showed a more specific uptake by the lymphatic system than ICG alone. By placing a region of interest over the liver, we were able to determine when the contrast agent had reached the bloodstream as both imaging agents distribute to this organ after i.v. injection (data not shown). As shown in Figure 2B, after intradermal injection of LP-ICG, enhancement peaks were seen in both draining lymph nodes before the liver showed enhancement at 60 to 70 min. In contrast, the ICG (Figure 2A) demonstrated much earlier enhancement at the liver (~10 min), suggesting partial uptake of the free dye by venous capillaries at the injection site and/or by high endothelial venules in the lymph nodes.

We also evaluated the clearance of LP-ICG from the injection site and from several tissues in mice after intradermal administration in comparison to ICG (Figure S4). No significant differences in tissue fluorescence were detected between LP-ICG injected animals versus ICG injected animals at 24h or 48h post-injection. At 48 h after injection, there was no significantly increased signal intensity in any of the evaluated tissues above normal values, indicating that LP-ICG is efficiently cleared with no evidence of retention by the reticuloendothelial system.

Imaging in *Chy* mutant mice after intradermal injection

The LP-ICG was then tested in a model of lymphatic dysfunction. *Chy* mice, which have a mutation in VEGFR3, lack dermal lymphatics and develop lymphedema in the hind paws (35). Three male *Chy* mice and three wild type littermates were injected with 5 μL of LP-ICG and sequential imaging was performed for 1 h. Images were also taken shortly after injection, at 4 h, and at 24 h to track clearance of the contrast agents from the injection site.

Representative sequential images after injection in *Chy* mice (Figure 3A, left panels) showed no enhancement of the popliteal or iliac lymph nodes for up to 1 h after imaging. There was additionally no signal increase in the liver, indicating that the liposomes remained confined to the interstitial space. Conversely, all wild type NMRI littermates showed rapid enhancement and flow through popliteal lymph nodes after injection (Figure 3A, right panels), with similar dynamics to those observed in normal albino C57BL/6 mice.

Evaluation of the clearance of LP-ICG in *Chy* mice at later timepoints indicated that despite the lack of dermal lymphatics, liposomes were cleared from the site of injection (Figure 3B, right panels). However, this process occurred at a reduced rate compared to wild type littermates. Whereas the signal intensity at the injection site was comparable in both groups at 10 min, there were significant differences at both 4 and 24 h after injection (Figure 3C). The clearance in *Chy* mice appeared to occur *via* interstitial diffusion as a diffuse

fluorescent signal shifted proximally up the hind limb at later timepoints (Figure 3B, left panels).

Lymphatic imaging in B16 tumor bearing animals

We next investigated whether LP-ICG could be used to quantify tumor-associated lymph flow. We hypothesized that lymphatic flow through tumor draining lymph nodes would be increased in comparison to normal nodes, and that tumors overexpressing VEGF-C would have a further acceleration in flow. To test this, B16-F10-luc2 mouse melanoma cells expressing luciferase were stably transfected with a human VEGF-C overexpression vector. After injection into the footpad of C57BL/6 albino mice, the dynamics of tumor growth were evaluated using bioluminescent (data not shown) and caliper measurements. No significant differences in tumor growth were found between tumors overexpressing VEGF-C or control vector (Figure 4A).

Tumors expressing high levels of VEGF-C have been shown to increase lymph node metastases (3–5,40). Thus, we next performed *in vivo* bioluminescent imaging of the popliteal lymph node region. No metastases were detected in either group at days 10 and 15. At day 21, an evaluation of *in vivo* bioluminescence intensity indicated a significant increase in popliteal lymph node signal in the VEGF-C group (Figure 4B). We found that 7/9 mice bearing VEGF-C overexpressing tumors had popliteal lymph node metastases (Figure 4C), while only 2/8 mice bearing pcDNA control tumors (Figure 4D) had metastases. These metastases rates are similar to those previously reported for the B16-F10 model (36). The luciferase signals of dissected lymph nodes detected ex vivo were comparable to the in vivo detected signals (Figures 4C and 4D, insets).

The lymphatic flow dynamics after peritumoral, intradermal injection of LP-ICG were then evaluated in VEGF-C overexpressing tumor bearing animals and compared to pcDNA tumor bearing and normal mice. To quantify the dynamics of flow, the data of signal intensity in the popliteal lymph node *versus* time were fitted to a model of exponential decay (Figure S5). Data analysis yielded the elimination (K_{LN}) constant and half-life of signal decay. It was found that pcDNA tumor bearing mice (Figure 5A, left) had increased lymphatic clearance through popliteal lymph nodes in comparison to non-tumor bearing animals. Surprisingly, the VEGF-C overexpressing tumor bearing mice had a much greater variability in clearance rates, with one group of mice showing rapid flow (Figure 5A, middle) and another showing dramatically reduced flow (Figure 5A, right). A direct comparison of the *in vivo* bioluminescence values of popliteal lymph node metastases to the K_{LN} values in VEGF-C tumor-bearing mice mice resulted in a negative correlation (Figure 5B, left, $p < 0.05$). By setting a threshold of average *in vivo* bioluminescence of the popliteal lymph nodes to 1×10^4 photons/s/cm^2/sr, we separated the VEGF-C tumor bearing mice into two groups, a low (or "early") metastatic burden group and a high metastatic burden group. With this threshold, it was found that low metastatic VEGF-C tumor bearing mice had accelerated lymphatic flow that was significantly higher than that in both non-tumor bearing mice and pcDNA tumor bearing mice (Figures 5, middle and right). In contrast, VEGF-C overexpressing tumor bearing mice with a higher metastatic burden in tumor draining lymph nodes had a much slower lymphatic flow, which was not significantly different from non-tumor bearing mice. Immunofluorescence stains for the melanoma cell marker gp100 demonstrated that large tumor cell masses could be found in the subcapsular sinus region of lymph nodes of mice with high metastatic burden (Figure S6). In comparison, lymph nodes from mice with a low metastatic burden revealed only few gp100 positive cells.

DISCUSSION

In this study, a novel near-infrared contrast system containing ICG was developed to image lymphatic flow and clearance in several mouse models. The LP-ICG formulation has several advantages over ICG including: (1) increased fluorescence signal with a shift towards the longer wavelength absorption and emission, (2) vastly improved stability in solution and biological fluids, (3) specific uptake into the lymphatic system, (4) increased clearance from the injection site with no retention in lymph nodes or other organs, and (5) improved visualization of deeper lymph nodes *in vivo*. These characteristics of LP-ICG have enabled development of quantifications of lymphatic function in mice.

ICG is considered one of the most attractive exogenous contrast agents for *in vivo* NIRF imaging, thanks to its spectral properties, minimal toxicity, low cost and FDA-approved status as a medical diagnostic compound (16). The design of an efficient ICG delivery system should preserve its optical properties and improve them whenever possible. The chemical and physical features of the molecule and the physiology of the target tissue have to be taken into consideration in the development process. For the current application, the formulation was optimized to include (a) a hydrophobic domain capable of preventing dye oligomerization, prolonging life-time and reducing self-quenching, (b) a flexible hydrophilic polymeric coating (PEG) to prevent phagocytosis after injection (41), and (c) a suitable size for specific uptake into lymphatic vessels. The optimized formulation (DOPC/PEG-DSPE 95:5 mol/mol, 60 nm) exhibited an increased absorbance, a bathochromic shift in the absorption spectrum and a total fluorescence yield ~4-fold higher than ICG. The spectral properties of LP-ICG were preserved in serum-containing media over the time range of the *in vivo* experiments. The low liposomal content release in low-serum medium indicates bilayer stability in the lymphatic fluids during the time course of the imaging studies.

After intradermal injection, the increased brightness of LP-ICG and the reduction of background signal due to the bathochromic shifts, along with specificity of uptake into the lymphatic system, allowed clear visualization of not only the popliteal lymph nodes, but also the medial iliac lymph nodes. These lymph nodes, downstream of the popliteal in the lymphatic drainage route from rear paws in mice (42), are located deep in the abdomen of the mouse (approximately 1 cm below the surface of the skin under the intestines), a region of high autofluorescence in the visible spectrum.

Unlike sentinel lymph node localization, in which it is considered to be advantageous to have the injected contrast agent retained by lymph node macrophages for sustained detection, we aimed to develop an agent that would passively flow through the lymphatic system. This feature is necessary to enable development of quantification methods of lymphatic flow with no interference from phagocytotic cells. It is generally accepted, mostly from experiences with lymphscintigraphy, that the ideal size for lymphatic uptake ranges from 5 to 100 nm (9). Smaller particles may be taken up by venous capillaries and enter the bloodstream directly. Larger particles cannot enter the endothelial cell junctions and may be retained for long periods at the site of injection (43). Instead of size, surface characteristics of liposomes play a more important role in lymph node retention (44–45). By coating the surface of the 60-nm LP-ICG with PEG, retention in the lymph nodes was avoided. In addition, LP-ICG was not retained in any other organ of the mice, similar to the clearance dynamics of ICG. Both the free ICG and the encapsulated ICG demonstrated no evidence of uptake by the reticuloendothelial system, and they were quickly cleared through the liver and bile, indicating that LP-ICG were destabilized once in the systemic circulation. This is an important difference in comparison to other nanoparticles tested as lymphatic tracers in animals. Quantum dots, even when coated with PEG, are retained in many organs after

injection (46). This efficient clearance, as well as the fact that all excipients used in this study are already used in humans, indicates a potential excellent safety profile for LP-ICG.

Our findings of increased lymphatic flow from murine melanoma tumors are consistent with recent studies using PEGylated quantum dots (38) or intravital microscopy methods (47). However, in our study, we collected sequential images, enabling clear visualization of the dynamics of signal at draining lymph nodes. By normalizing our measures of signal intensity of ICG to a peak enhancement value, we were able to develop a novel quantification method based on an exponential decay model over time that revealed significant increases in lymphatic flow from B16 tumors compared to non-tumor bearing animals.

NIRF imaging with LP-ICG could be combined with bioluminescence imaging of luciferase expressing tumor cells during a single imaging session to assess lymphatic flow, primary tumor bioluminescent signal, and lymph node metastases. The noninvasive nature of these modalities, as well as the fact that LP-ICG clears rapidly from the mouse, enables longitudinal imaging to be performed in the same animal. These methods will be powerful new tools to test novel therapeutic agents intended to improve or decrease lymphatic function in preclinical studies.

The combined bioluminescent/fluorescent imaging revealed an interesting phenomenon in mice with an increased lymph node tumor burden. The clearance rates of LP-ICG through the draining lymph nodes in these mice were dramatically reduced in comparison to tumor bearing animals with low lymph node tumor cell burden. It has been well-described that tumor cells after metastasizing through lymphatics seed in subcapsular sinuses of the lymph node (47–48), in agreement with our findings (Figure S6). It is conceivable that proliferation of tumor cells at this location could hinder flow of the liposomes through the lymph node. A similar phenomenon has been reported in several clinical studies during sentinel lymph node mapping in which total occlusion by tumor cells prevents blue dye and/or radioisotopes from identifying sentinel nodes (49–50). We are currently undertaking further studies to evaluate whether similar methods may be sensitive to predict which draining lymph nodes are positive for tumor cells. With the recent development of intraoperative NIR imaging systems (51), there may be a possibility to evaluate liposome-based contrast agent drainage patterns during surgery to improve the sensitivity of sentinel lymph node detection.

Supplementary Material

Refer to Web version on PubMed Central for supplementary material.

Acknowledgments

REFERENCES

1. Karpanen T, Alitalo K. Molecular biology and pathology of lymphangiogenesis. Annu Rev Pathol. 2008; 3:367–397. [PubMed: 18039141]
2. Jurisic G, Detmar M. Lymphatic endothelium in health and disease. Cell Tissue Res. 2009; 335:97–108. [PubMed: 18648856]

3. Mattila MM-T, Ruohola JK, Karpanen T, Jackson DG, Alitalo K, Härkönen PL. VEGF-C induced lymphangiogenesis is associated with lymph node metastasis in orthotopic MCF-7 tumors. Int J Cancer. 2002; 98:946–951. [PubMed: 11948478]

4. Mumprecht V, Detmar M. Lymphangiogenesis and cancer metastasis. J Cell Mol Med. 2009; 13:1405–1416. [PubMed: 19583813]

5. Skobe M, Hawighorst T, Jackson DG, et al. Induction of tumor lymphangiogenesis by VEGF-C promotes breast cancer metastasis. Nat Med. 2001; 7:192–198. [PubMed: 11175850]

6. Hirakawa S, Kodama S, Kunstfeld R, Kajiya K, Brown LF, Detmar M. VEGF-A induces tumor and sentinel lymph node lymphangiogenesis and promotes lymphatic metastasis. J Exp Med. 2005; 201:1089–1099. [PubMed: 15809353]

7. Hirakawa S, Brown LF, Kodama S, Paavonen K, Alitalo K, Detmar M. VEGF-C-induced lymphangiogenesis in sentinel lymph nodes promotes tumor metastasis to distant sites. Blood. 2007; 109:1010–1017. [PubMed: 17032920]

8. Van den Eynden GG, Smid M, Van Laere SJ, et al. Gene Expression Profiles Associated with the Presence of a Fibrotic Focus and the Growth Pattern in Lymph Node–Negative Breast Cancer. Clin Cancer Res. 2008; 14:2944–2952. [PubMed: 18483361]

9. Barrett T, Choyke P, Kobayashi H. Imaging of the lymphatic system: new horizons. Contrast Media Mol Imaging. 2006; 1:230–245. [PubMed: 17191764]

10. Kobayashi H, Kawamoto S, Bernardo M, Brechbiel M, Knopp M, Choyke P. Delivery of gadolinium-labeled nanoparticles to the sentinel lymph node: Comparison of the sentinel node visualization and estimations of intra-nodal gadolinium concentration by the magnetic resonance imaging. J Control Release. 2006; 111:343–351. [PubMed: 16490277]

11. Kobayashi H, Kawamoto S, Star R, Waldmann T, Tagaya Y, Brechbiel M. Micro-magnetic resonance lymphangiography in mice using a novel dendrimer-based magnetic resonance imaging contrast agent. Cancer Res. 2003; 63:271–276. [PubMed: 12543772]

12. Wunderbaldinger P, Josephson L, Bremer C, Moore A, Weissleder R. Detection of lymph node metastases by contrast-enhanced MRI in an experimental model. Magn Reson Med. 2002; 47:292–297. [PubMed: 11810672]

13. Misselwitz B. MR contrast agents in lymph node imaging. Eur J Radiol. 2006; 58:375–382. [PubMed: 16464554]

14. Herborn C, Lauenstein T, Vogt F, Lauffer RB, Debatin JF, Ruehm SG. Interstitial MR lymphography with MS-325: characterization of normal and tumor-invaded lymph nodes in a rabbit model. Am J Roentgenol. 2002; 179:1567–1572. [PubMed: 12438057]

15. Rasmussen JC, Tan I-C, Marshall MV, Fife CE, Sevick-Muraca EM. Lymphatic imaging in humans with near-infrared fluorescence. Curr Opin Biotechnol. 2009; 20:74–82. [PubMed: 19233639]

16. Frangioni JV. In vivo near-infrared fluorescence imaging. Curr Opin Chem Biol. 2003; 7:626–634. [PubMed: 14580568]

17. Rao J, Dragulescuandrasi A, Yao H. Fluorescence imaging in vivo: recent advances. Curr Opin Biotechnol. 2007; 18:17–25. [PubMed: 17234399]

18. Cherrick GR, Stein SW, Leevy CM, Davidson CS. Indocyanine green: observations on its physical properties, plasma decay, and hepatic extraction. J Clin Invest. 1960; 39:592–600. [PubMed: 13809697]

19. Saxena V, Sadoqi M, Shao J. Degradation kinetics of indocyanine green in aqueous solution. J Pharm Sci. 2003; 92:2090–2097. [PubMed: 14502548]

20. Sharma R, Wang W, Rasmussen JC, et al. Quantitative imaging of lymph function. Am J Physiol Heart Circ Physiol. 2007; 292:H3109–H3118. [PubMed: 17307997]

21. Unno N, Nishiyama M, Suzuki M, et al. Quantitative Lymph Imaging for Assessment of Lymph Function using Indocyanine Green Fluorescence Lymphography. Eur J Vasc Endovasc Surg. 2008; 36:230–236. [PubMed: 18534875]

22. Sharma R, Wendt JA, Rasmussen JC, Adams KE, Marshall MV, Sevick-Muraca EM. New horizons for imaging lymphatic function. Ann NY Acad Sci. 2008; 1131:13–36. [PubMed: 18519956]

23. Saxena V, Sadoqi M, Shao J. Indocyanine green-loaded biodegradable nanoparticles: preparation, physicochemical characterization and in vitro release. Int J Pharm. 2004; 278:293–301. [PubMed: 15196634]

24. Devoisselle J-M, Soulie-Begu S, Maillols H, Desmettre T, Mordon SR. Fluorescence properties of indocyanin green: II. In-vitro study related to in-vivo behavior SPIE, Advances in Fluorescence Sensing Technology III. 1997; 2980:293–302.

25. Mordon S, Devoisselle JM, Soulie-Begu S, Desmettre T. Indocyanine green: physicochemical factors affecting its fluorescence in vivo. Microvasc Res. 1998; 55:146–152. [PubMed: 9521889]

26. Moody ED, Viskari PJ, Colyer CL. Non-covalent labeling of human serum albumin with indocyanine green: a study by capillary electrophoresis with diode laser-induced fluorescence detection. J Chromatogr B Biomed Sci Appl. 1999; 729:55–64. [PubMed: 10410927]

27. Ohnishi S, Lomnes SJ, Laurence RG, Gogbashian A, Mariani G, Frangioni JV. Organic alternatives to quantum dots for intraoperative near-infrared fluorescent sentinel lymph node mapping. Mol Imaging. 2005; 4:172–181. [PubMed: 16194449]

28. Sadoqi, M.; Kumar, S.; Lau-Cam, C.; Saxena, V. Biocompatible nanoparticulate systems for tumor diagnosis and therapy. In: Kumar, CSSR., editor. Nanotechnologies for Life Sciences. Weinheim: Wiley-VCH Verlag GmbH & Co.; 2006. p. 304-348.

29. Bahner, M.; Haag, R.; Heek, T.; Licha, K.; Schirner, M.; Wyszogrodzka, M.; Mivenion, GmbH. New polyether polyol dendron conjugate comprises a polyether polyol dendron moiety, and at least one effector molecule, e.g. fluorescent dyes, useful for treating or diagnosing a disease state or condition, e.g. tumors and atherosclerosis. WO2009112488-A2. 2009 Sep 16. inventors assignee

30. Devoisselle J-M, Soulie-Begu S, Mordon SR, Desmettre T, Maillols H. Fluorescence properties of indocyanin green: I. In-vitro study with micelles and liposomes. SPIE, Advances in Fluorescence Sensing Technology III. 1997; 2980:453–460.

31. Kirchherr A-K, Briel A, Mäder K. Stabilization of Indocyanine Green by Encapsulation within Micellar Systems. Mol Pharm. 2009; 6:480–491. [PubMed: 19228053]

32. Lasic DD. Novel applications of liposomes. Trends Biotechnol. 1998; 16:307–321. [PubMed: 9675915]

33. Hope MJ, Bally MB, Webb G, Cullis PR. Characterization of size distribution, trapped volume and ability to maintain a membrane potential. Biochim Biophys Acta. 1985; 812:55–65.

34. Pfohl T, Riegler H. Critical Wetting of a liquid/vapor interface by octane. Phys Rev Lett. 1999; 82:783.

35. Karlsen TV, Karkkainen MJ, Alitalo K, Wiig H. Transcapillary fluid balance consequences of missing initial lymphatics studied in a mouse model of primary lymphoedema. J Physiol. 2006; 574:583–596. [PubMed: 16675495]

36. Li J, Wang E, Rinaldo F, Datta K. Upregulation of VEGF-C by androgen depletion: the involvement of IGF-IR-FOXO pathway. Oncogene. 2005; 24:5510–5520. [PubMed: 15897888]

37. Tuomela J, Valta M, Seppanen J, Tarkkonen K, Vaananen HK, Harkonen P. Overexpression of vascular endothelial growth factor C increases growth and alters the metastatic pattern of orthotopic PC-3 prostate tumors. BMC Cancer. 2009; 9:362. [PubMed: 19821979]

38. Harrell MI, Iritani BM, Ruddell A. Tumor-induced sentinel lymph node lymphangiogenesis and increased lymph flow precede melanoma metastasis. Am J Pathol. 2007; 170:774–786. [PubMed: 17255343]

39. Vandenbroeck W, Derore A, Simoens P. Anatomy and nomenclature of murine lymph nodes: Descriptive study and nomenclatory standardization in BALB/cAnNCrl mice. J Immunol Methods. 2006; 312:12–19. [PubMed: 16624319]

40. Karpanen T, Egeblad M, Karkkainen MJ, et al. Vascular endothelial growth factor C promotes tumor lymphangiogenesis and intralymphatic tumor growth. Cancer Res. 2001; 61:1786–1790. [PubMed: 11280723]

41. Lasic DD, Martin FJ, Gabizon A, Huang SK, Papahadjopoulos D. Sterically stabilized liposomes: a hypothesis on the molecular origin of the extended circulation times. Biochim Biophys Acta. 1991; 1070:187–192. [PubMed: 1751525]

42. Harrell MI, Iritani BM, Ruddell A. Lymph node mapping in the mouse. J Immunol Methods. 2008; 332:170–174. [PubMed: 18164026]

43. Weissleder R, Thrall JH. The lymphatic system: diagnostic imaging studies. Radiology. 1989; 172:315–317. [PubMed: 2748809]

44. Oussoren C, Storm G. Liposomes to target the lymphatics by subcutaneous administration. Adv Drug Deliv Rev. 2001; 50:143–156. [PubMed: 11489337]

45. Phillips, WT.; Goins, BA.; Medina, LA. Targeting of liposomes to lymph nodes. In: Gregoriadis, G., editor. Liposome Technology. 3rd Edition. New York, N. Y: Informa Healthcare; 2007. p. 231-252.

46. Ballou B, Lagerholm BC, Ernst LA, Bruchez MP, Waggoner AS. Noninvasive imaging of quantum dots in mice. Bioconjug Chem. 2004; 15:79–86. [PubMed: 14733586]

47. Hoshida T, Isaka N, Hagendoorn J, et al. Imaging steps of lymphatic metastasis reveals that vascular endothelial growth factor-C increases metastasis by increasing delivery of cancer cells to lymph nodes: therapeutic implications. Cancer Res. 2006; 66:8065–8075. [PubMed: 16912183]

48. Hayashi K, Jiang P, Yamauchi K, et al. Real-time imaging of tumor-cell shedding and trafficking in lymphatic channels. Cancer Res. 2007; 67:8223–8228. [PubMed: 17804736]

49. Goyal A, Douglas-Jones AG, Newcombe RG, Mansel RE. Effect of lymphatic tumor burden on sentinel lymph node biopsy in breast cancer. Breast J. 2005; 11:188–194. [PubMed: 15871704]

50. Wong SL, Edwards MJ, Chao C, Simpson D, McMasters KM. The effect of lymphatic tumor burden on sentinel lymph node biopsy results. Breast J. 2002; 8:192–198. [PubMed: 12100110]

51. Tanaka E, Choi HS, Fujii H, Bawendi MG, Frangioni JV. Image-guided oncologic surgery using invisible light: completed pre-clinical development for sentinel lymph node mapping. Ann Surg Oncol. 2006; 13:1671–1681. [PubMed: 17009138]
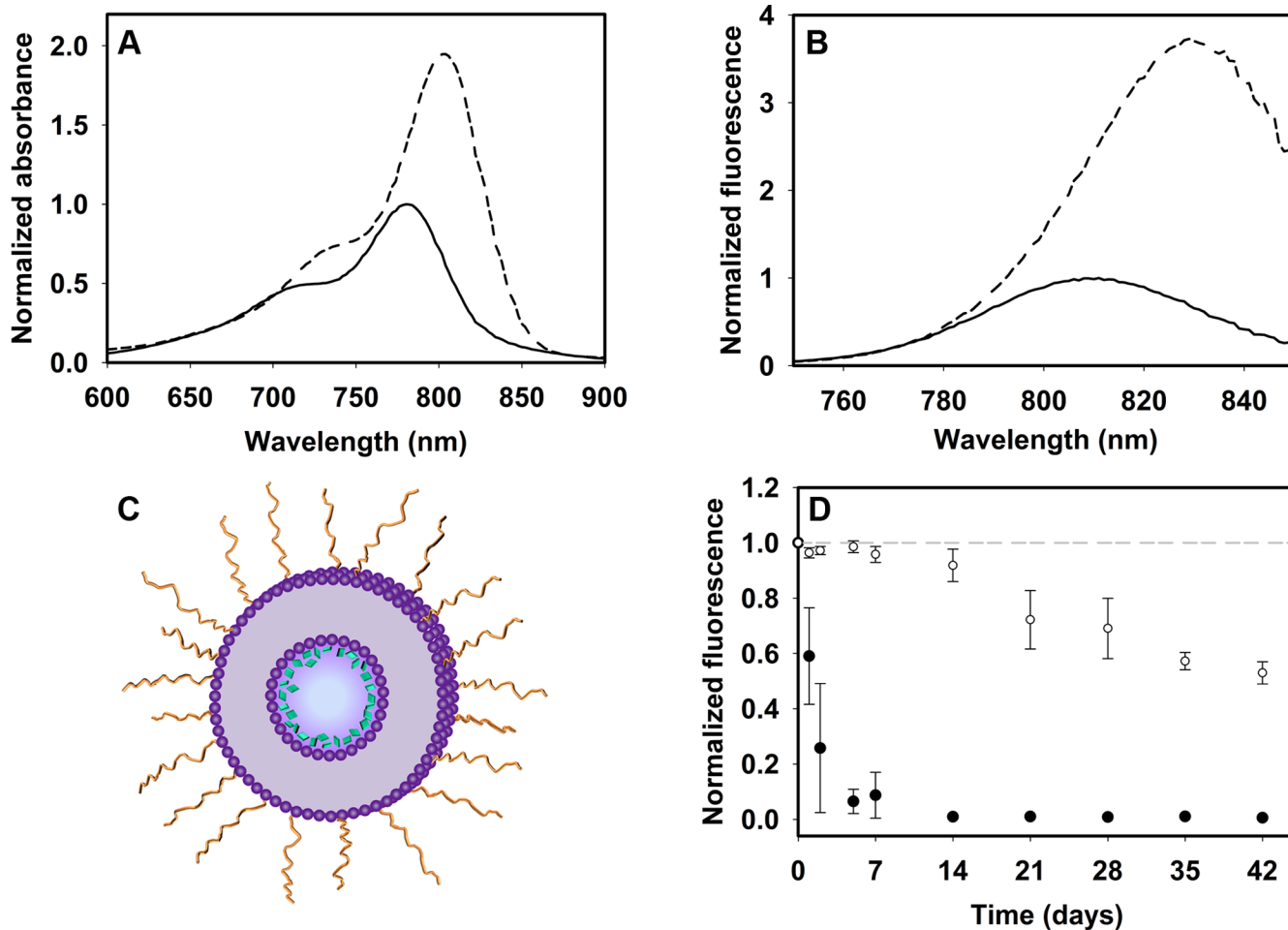
Figure 1. Spectral properties of LP-ICG

Typical normalized absorption (A) and fluorescence (B) spectra of LP-ICG (C) with respect to free ICG. Solid line: ICG in 5% glucose; dashed line: LP-ICG. The spectra are normalized for the maximum absorbance (λ_{max} = 780 nm) and the maximum fluorescence emission (λ_{max} = 810 nm) of free ICG. The stability of the spectral properties of LP-ICG over time is compared to that of ICG in buffer. The fluorescence maximum emission over time (D) is normalized for the initial maximum emission (ICG λ_{em} = 810 nm; LP-ICG λ_{em} = 831 nm). Filled circles: ICG; empty circles: LP-ICG.
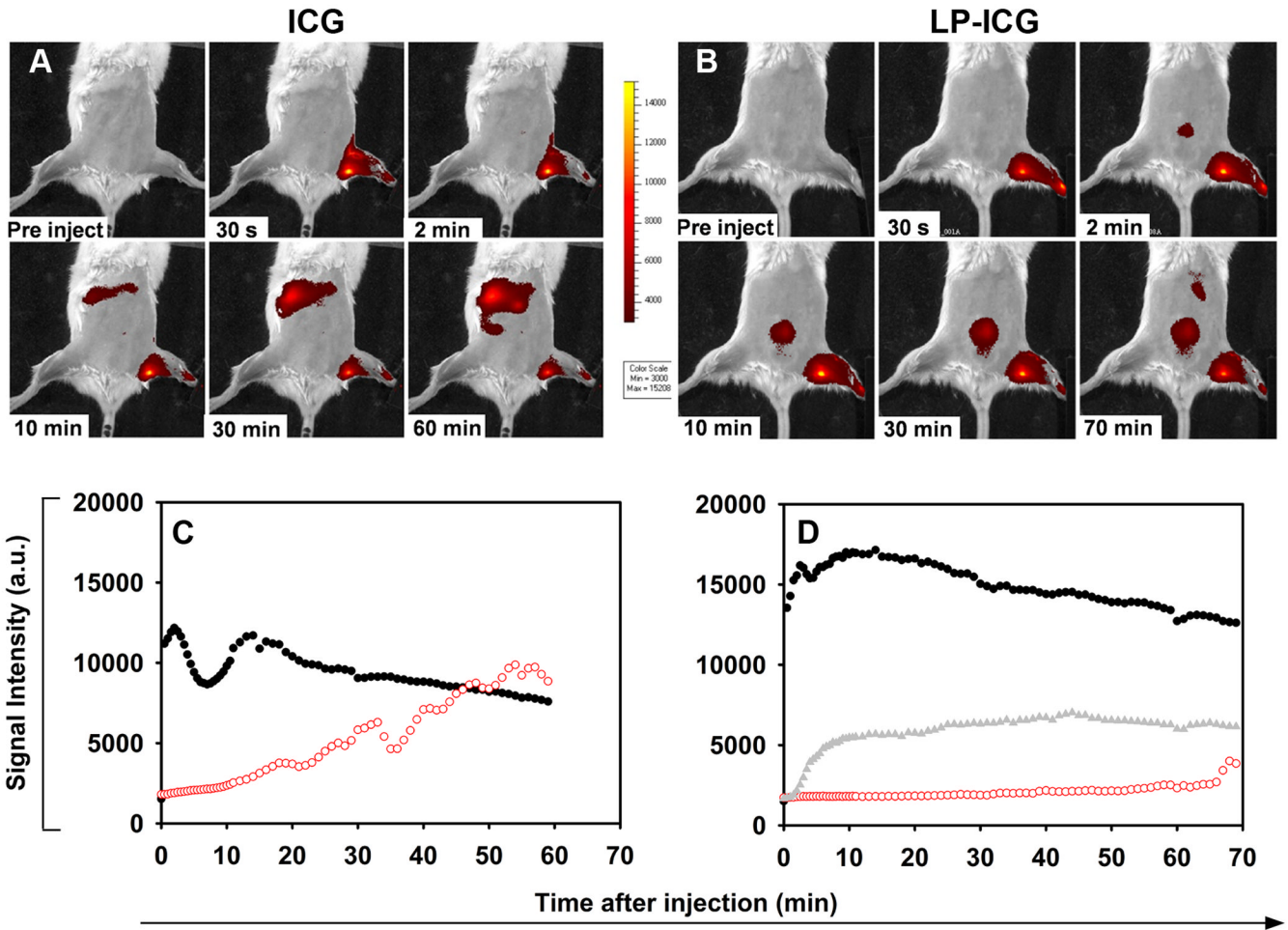
Figure 2. Dynamics of ICG signal after intradermal injection in normal C57BL/6 albino mice
Time series of images from representative animals before and after intradermal injection of the left rear paw with ICG (A) and LP-ICG (B). Images were collected with 4-s exposure time in both animals. Enhancement of popliteal lymph node and liver are seen in (A) and (B), while the medial iliac lymph node shows also signal enhancement in (B). Signal intensity of enhanced tissues is plotted *versus* time in ICG (C) and LP-ICG (D) injected mice. Black circles: popliteal lymph node; red squares: liver; grey triangles: medial iliac lymph node.
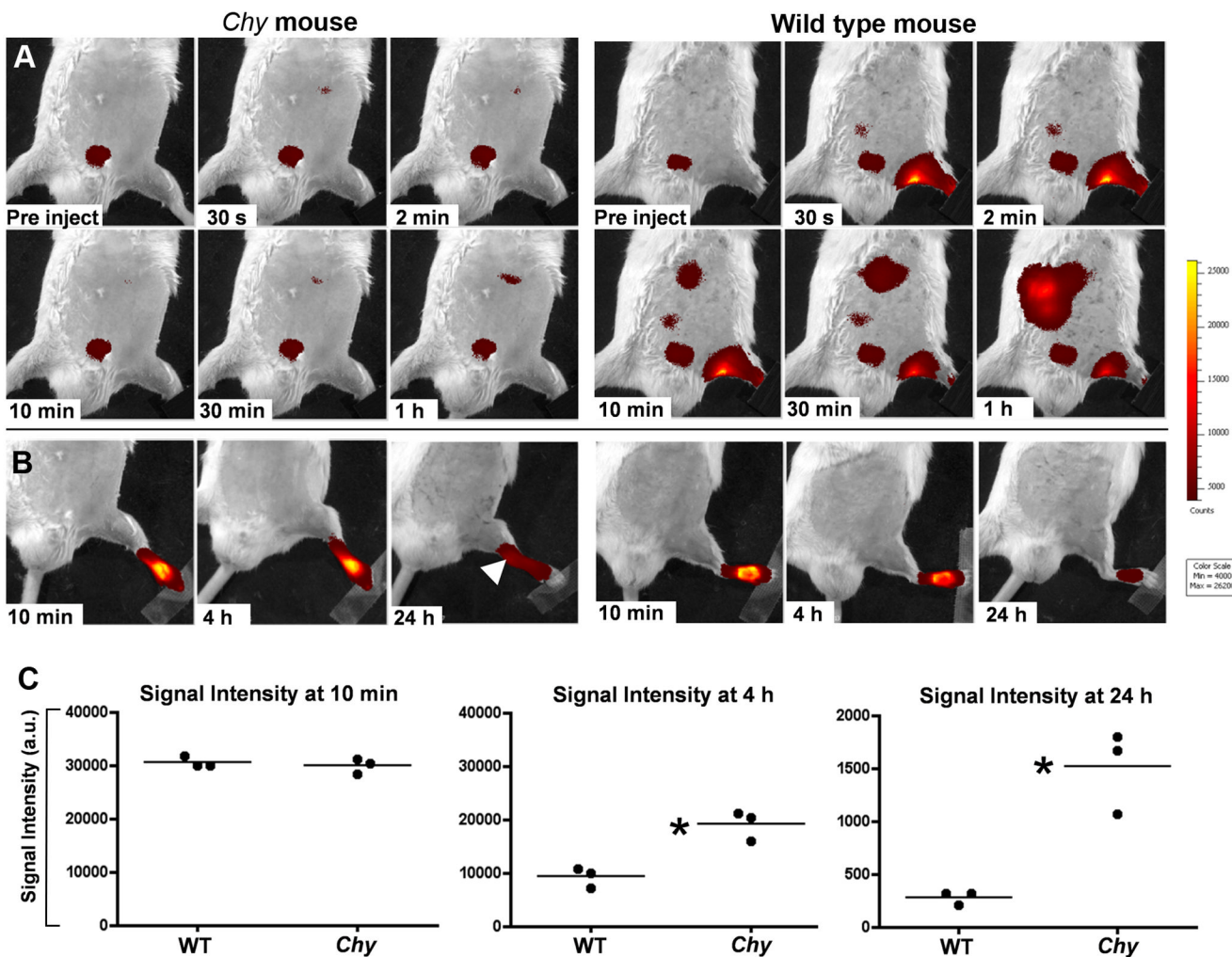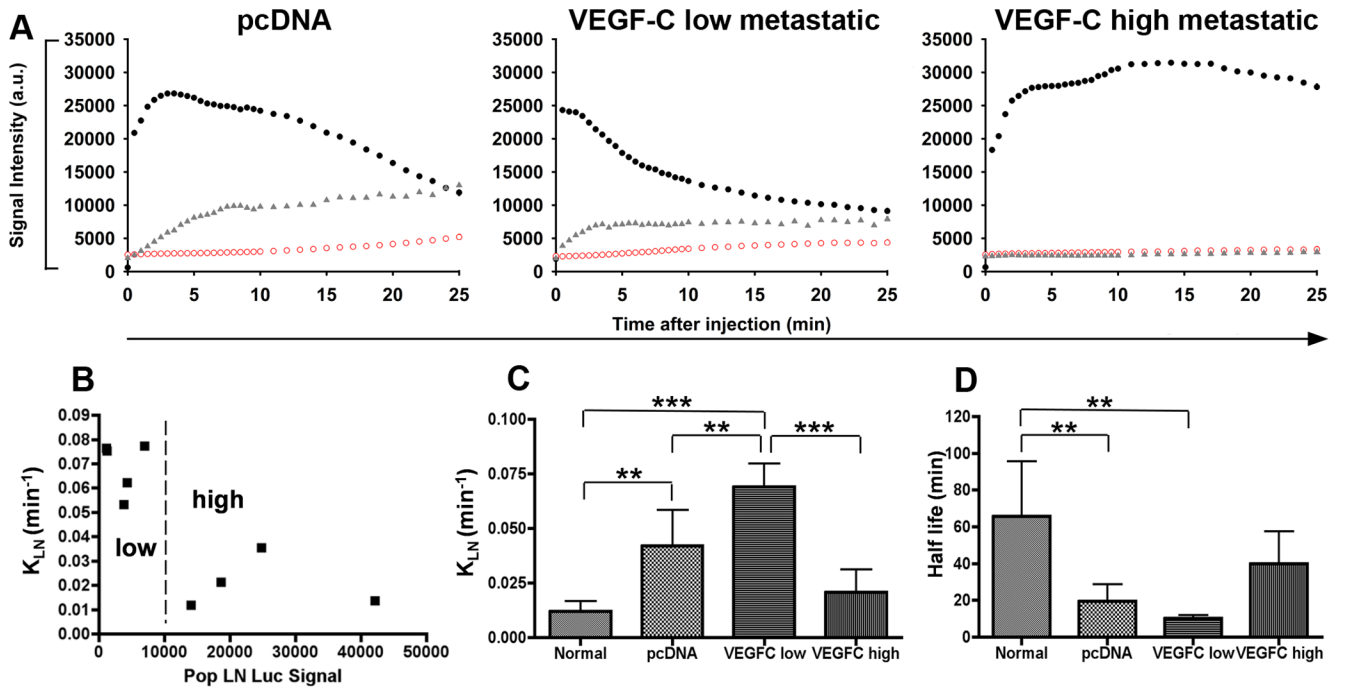
Figure 3. NIRF imaging of *Chy* mice after intradermal injection
Time series of images (exposure time 6 s) after intradermal injection of LP-ICG in a
representative 5 month old male *Chy* mouse (A, left) and wild type littermate (A, right).
Images of injection site (exposure time 0.1 s) taken 10 min, 4 h, and 24 h after injection into
foot of a representative *Chy* mouse (B, left) and wild type littermate (B, right). White
arrowhead at 24 h in (B, left) shows interstitial diffusion pattern from foot in *Chy* mouse. In
C, scatter plots of signal intensity measurements of injected feet at 10 min, 4 h, and 24 h. * p
< 0.05
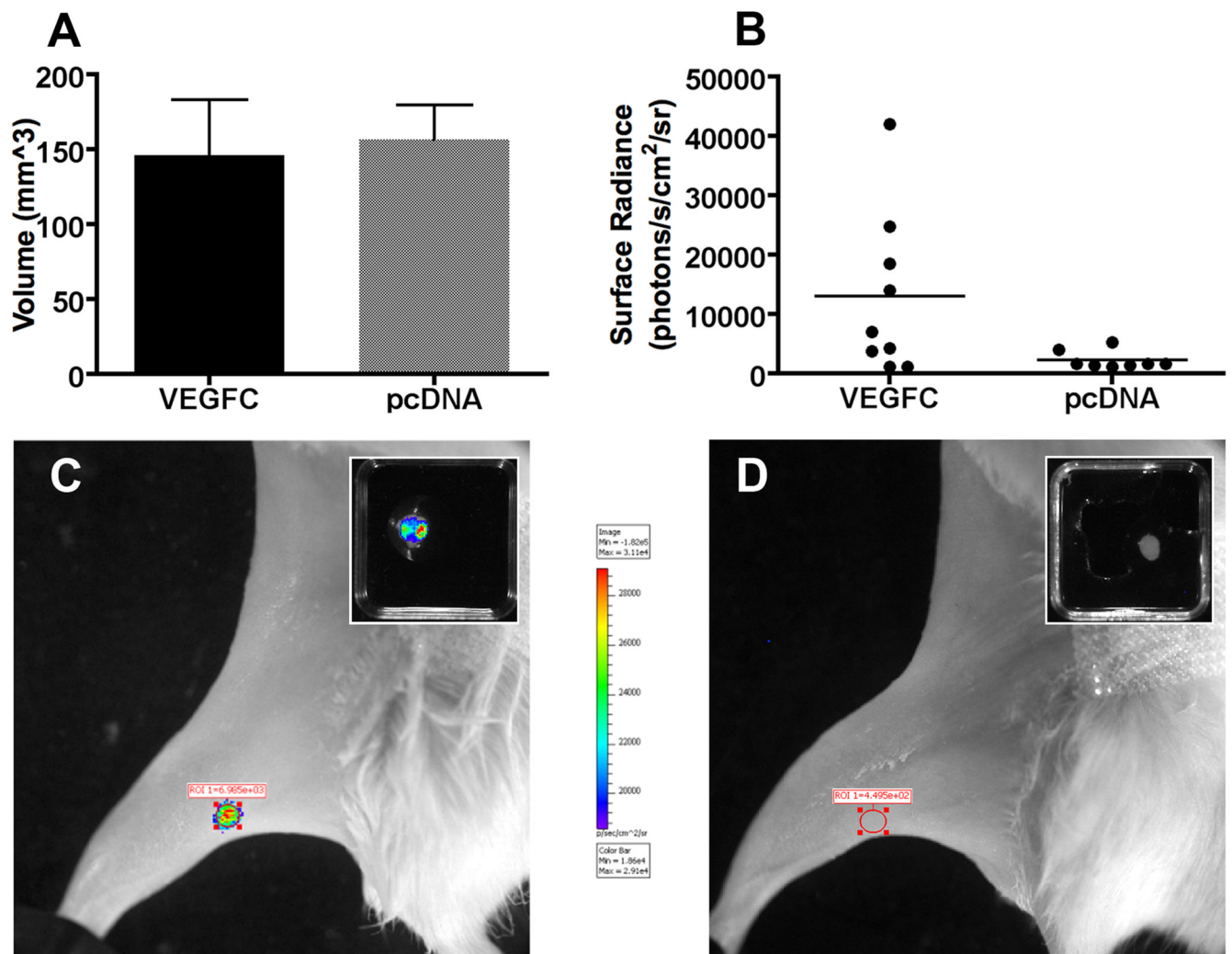
Figure 4. Bioluminescent imaging of popliteal lymph node metastases in human VEGF-C overexpressing B16-luc2 melanoma tumor bearing mice
(A) Tumor volumes of VEGF-C expressing and control cells at 21 days. Quantification of *in vivo* bioluminescent signals from 9 VEGF-C and 8 pcDNA tumor bearing mice (B). Bioluminescent images of popliteal lymph node region revealing lymph node metastasis in representative VEGF-C tumor bearing mouse (C) and lack of signal in pcDNA tumor bearing mouse (D). Insets: *Ex vivo* signal of dissected popliteal lymph nodes from VEGF-C (C) or pcDNA (D) tumor bearing mice. * $p < 0.05$

Figure 5. Dynamic NIRF imaging of ICG liposome injected B16-luc2 tumor bearing mice
Representative figures of lymphatic drainage patterns of LP-ICG after intradermal injection
(A) from pcDNA, VEGF-C low metastatic, and VEGF-C high metastatic mice. Black
circles: popliteal lymph node; red squares: liver; grey triangles: medial iliac lymph node.
Correlation plot (B) showing K_{LN} rates through popliteal lymph node *versus* popliteal
lymph node luciferase signals. Dashed line represents threshold between low metastatic and
high metastatic VEGF-C tumor bearing mice. K_{LN} rates (C) and half life measurements (D)
of normal, pcDNA tumor, VEGF-C low metastatic and VEGF-C high metastatic groups. * p
< 0.05, ** p < 0.01, *** p < 0.001.